Available online at www.sciencedirect.com
ScienceDirect
Current Opinion in Solid State and Materials Science 10 (2006) 93–107
Current Opinion in Solid State & Materials Science

Heusler alloy/semiconductor hybrid structures

A. Hirohata [a,*], M. Kikuchi [b,c], N. Tezuka [b,d], K. Inomata [b,d], J.S. Claydon [e], Y.B. Xu [e], G. van der Laan [f]

[a] Frontier Research System, RIKEN, 2-1 Hirosawa, Wako 351-0198, Japan
[b] Department of Materials Science, Graduate School of Engineering, Tohoku University, Sendai 980-8579, Japan
[c] Kojundo Chemical Laboratory, 5-1-28 Chiyoda, Sakado 350-0284, Japan
[d] CREST, Japan Science and Technology Agency, 4-1-8 Honcho, Kawaguchi 332-0012, Japan
[e] Department of Electronics, University of York, Heslington, York YO10 5DD, United Kingdom
[f] Magnetic Spectroscopy, Daresbury Laboratory, Warrington WA4 4AD, United Kingdom

Received 13 February 2006; accepted 15 November 2006

Abstract

Heusler alloys are theoretically predicted to become half-metals at room temperature (RT). The advantages of using these alloys are good lattice matching with III–V semiconductors, high Curie temperature above RT and intermetallic controllability for spin density of states at the Fermi level. These alloys are categorized into half and full Heusler alloys dependent upon the crystalline structures, each of which is discussed both experimentally and theoretically in Sections 2 and 3, respectively. As an example, our recent studies on epitaxial $L2_1$ Co_2 $Cr_{1-x}Fe_xAl(001)$/GaAs(001) hybrid structures are presented here. Both structural and magnetic characterizations on an atomic scale are typically carried out in order to prove the half-metallicity at RT as described in Section 4. Atomic ordering in the Heusler films is directly observed by X-ray diffraction and is also indirectly measured by the temperature dependence of electrical resistivity. Element specific magnetic moments and spin polarization of the Heusler alloy films are directly estimated by using X-ray magnetic circular dichroism and Andreev reflection, respectively. By employing these alloy films in a spintronic device, diffusive spin-polarized electron transport may offer highly efficient spin injection across a direct interface between the Heusler alloy film and the semiconductor, while ballistic transport in a magnetic tunnel junction may further improve areal density of a magnetic random access memory with a large magnetoresistance ratio at RT as discussed in Section 5. A brief summary is provided at the end of this review.

PACS: 71.20.Lp; 72.25.Ba; 75.70.−i

Keywords: Heusler alloy; Half-metallic ferromagnet; Spin polarization; Magnetic moment; Atomic disorder; Curie temperature; Minority bandgap

1. Introduction

The hybridization of a ferromagnetic metal with a semiconductor offers opportunities for engineering electron spin density of states (DOS) of the ferromagnet by tuning its lattice constant. A III–V semiconductor, in particular, has been utilized as a template for epitaxial growth of the ferromagnetic metals due to its relevant lattice constant matching. From the 1980s, by using a molecular-beam epitaxy (MBE) technique, ferromagnet/semiconductor direct interfacial properties, such as detailed growth modes, self organization, interfacial spin scattering and formation of magnetic dead layers, have been widely investigated in e.g., single-crystal epitaxial Fe/GaAs and Co/GaAs hybrid structures [1].

Simultaneously the search for an applicable spin-filtering layer has successfully produced very large tunnel magnetoresistance (TMR) with using a large Zeeman splitting in magnetic semiconductors, EuO and EuS [2]. Later, MBE-grown epitaxial dilute magnetic semiconductors

* Corresponding author. Tel.: +81 48 467 9607; fax: +81 467 9650.
E-mail address: ahirohata@riken.jp (A. Hirohata).

1359-0286/$ - see front matter © 2006 Elsevier Ltd. All rights reserved.
doi:10.1016/j.cossms.2006.11.006

(DMSs), such as (Ga,Mn)As and Zn(Be,Mn)Se, have demonstrated highly efficient spin injection into GaAs [3], which has been applied to the realization of spin-polarized three-terminal devices; a spin-polarized field effect transistor (spin FET) [4], a spin-polarized light-emitting diode (spin-LED) [3,5] and a spin-polarized resonant tunnel diode (spin RTD) [6]. However, the DMS requires a large external magnetic field to induce the Zeeman splitting at low temperature.

In order to exploit 100% spin polarization induced by spontaneous magnetization, half-metallic FMs (HMFs) have been intensively investigated recently [7]. The HMF possesses a bandgap δ at the Fermi level E_F only for its minority spins, achieving 100% spin polarization at E_F (see Fig. 1). Four types of the HMFs have theoretically been predicted so far; oxide compounds (e.g., rutile CrO_2 [8] and spinel Fe_3O_4 [9]), perovskites (e.g., (La,Sr)MnO_3 [10]), Zinc-blende compounds (e.g., CrAs [11]) and Heusler alloys (e.g., NiMnSb [12]). Even though both CrO_2 and $La_{0.7}Sr_{0.3}MnO_3$ have been reported to show almost 100% spin polarization at low temperature [13], to date there has been no experimental report on the half-metallicity at room temperature (RT), which is highly required from the viewpoint of device applications.

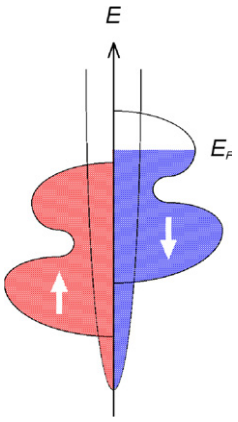

Fig. 1. Schematic diagram of density of states for a half-metallic ferromagnet.

Among these proposed HMFs, the Heusler alloys holds the greatest potential to realize the half-metallicity at RT due to their lattice constant matching with the III–V semiconductors, high Curie temperature T_C above RT and large δ at E_F in general. The Heusler alloys are categorized into two distinct groups by their crystalline structures; half Heusler alloys with the form of XYZ in the $C1_b$ structure and full Heusler alloys with the form of X_2YZ in the $L2_1$ structure as schematically drawn in Fig. 2(a) and (b), respectively, where X and Y atoms are transition metals, while Z is either a semiconductor or a non-magnetic metal (see Fig. 3) [12,14]. The unit cell of the $L2_1$ structure consists of four face-centered cubic (fcc) sublattices, while that of the $C1_b$ structure is formed by removing one of the X sites. In the Heusler alloys, the half-metallicity is known to be fragile against atomic disorder. For the $L2_1$ structure, when the Y and Z atoms replace their sites (Y–Z disorder) and eventually occupy their sites absolutely at random, the alloy transforms into the $B2$ structure (Fig. 2(c)). In addition, X–Y and X–Z disorder finally forms the $A2$ structure (Fig. 2(d)).

As shown in Fig. 4, most of both the half and full Heusler alloys possess their lattice constants in the range of those of the major III–V semiconductors, clearly indicating the possibilities of epitaxial growth. Co-based full Heusler

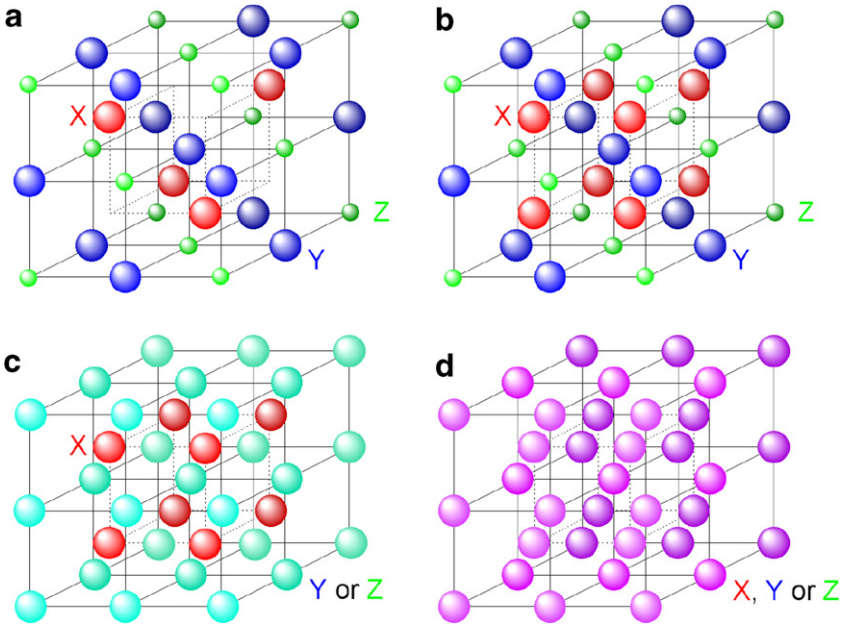

Fig. 2. Crystalline structures of both (a) half and (b) full Heusler alloys; $C1_b$ and $L2_1$ structures, respectively. Atomically disordered structures, (c) $B2$ and (d) $A2$, are also shown. After [14].

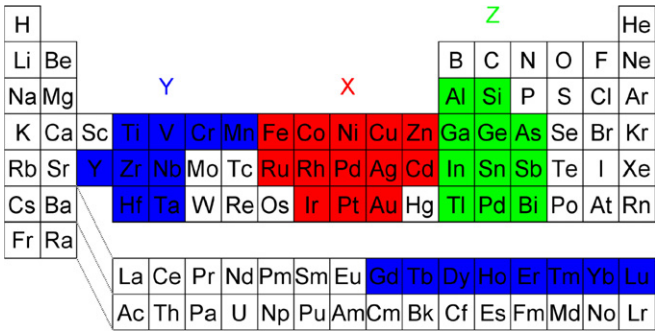

Fig. 3. Major combinations of Heusler alloy formation. After [14].

alloys especially hold excellent match with both GaAs and InAs compounds. The lattice constant can be further adjusted to an appropriate value by substituting the element X with a different atom as indicated as lines in Fig. 4, and also by substituting the other elements Y or Z with the other atoms as categorized in Fig. 3 with retaining the element X (e.g., $Co_2(Cr,Fe)Al$). Such crystallographical engineering approach is a powerful method to control the spin DOS in a unit cell to achieve robust half-metallicity at RT.

In addition, the T_C of the Heusler alloys falls typically within the range of 200 and 1200 K (see Fig. 5). The T_C can also be tuned to be above RT by the crystallographical element substitution as described above, achieving sufficient spontaneous magnetization at RT for the applications.

The origin of the bandgap in the Heusler alloys is attributed to the strong d-band hybridization of the two transition metals X and Y. According to the calculations by Galanakis et al. [19], the local DOS in the vicinity of E_F is dominated by the d-states, forming an energy gap between the higher degenerate of bonding hybridized states in the valence band and the lower degenerate of antibonding states in the conduction band. For the half Heusler alloys (Fig. 6(a)), the gap is formed between the hybridized states of the elements X and Y, i.e., between the three-fold degenerate (t_{2g}) in the bonding states and the two-fold degenerate (e_g) in the antibonding states. Therefore, most of the half Heusler alloys possess an indirect bandgap between the valence band minimum at the Γ point and the conduction maximum at the X point. For the full Heusler alloys, on the other hand, the d-band hybridization between the elements X plays a very important role,

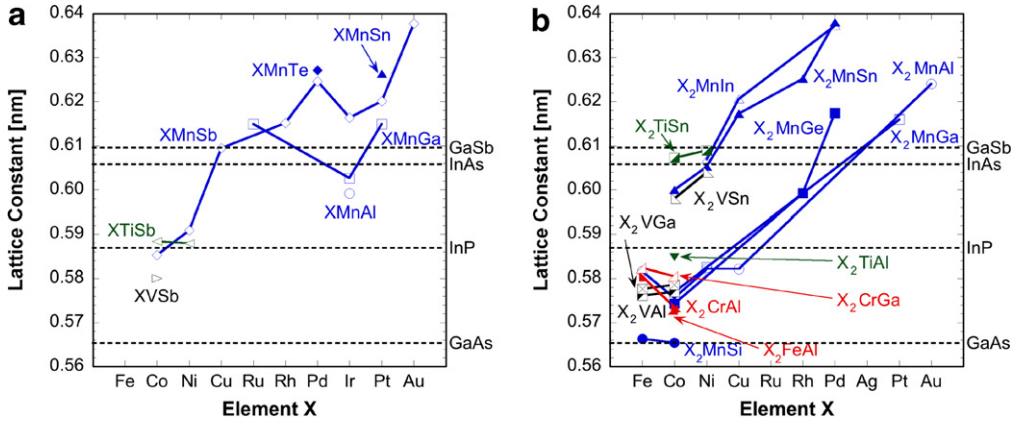

Fig. 4. Lattice constant distribution of both (a) half and (b) full Heusler bulk alloys with respect to the element X. Experimental data are used from Refs. [14–16]. Lattice constants of representative III–V semiconductors are also shown as references.

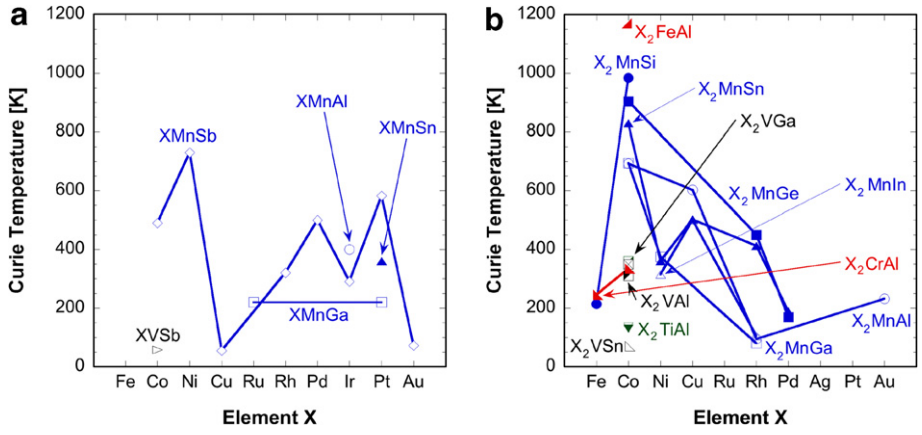

Fig. 5. Curie temperature distribution of both (a) half and (b) full Heusler bulk alloys with respect to the element X. Experimental data are used from Refs. [14,15,17].

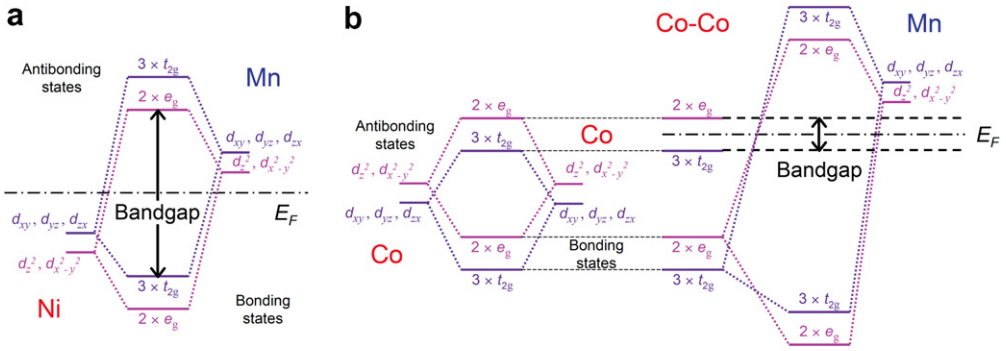

Fig. 6. Schematic illustrations of the origin of the minority bandgap in (a) half and (b) full Heusler alloys (NiMnZ and Co_2MnZ as examples, respectively) [19].

although these atoms occupy the second nearest neighbor sites (see Fig. 2(b)). As shown in Fig. 6(b), the X–X hybridization initially forms both bonding and antibonding states for both t_{2g} and e_g. The two bonding states among these four X–X orbitals then hybridize with the Y degenerates, developing both bonding and antibonding degenerates with a very large gap in between. The two X–X antibonding states, however, cannot couple with the Y degenerates, maintaining the small gap across E_F, which defines the bandgap for the full Heusler alloys. This can provide either a direct bandgap at the Γ point or an indirect bandgap between the Γ and X points.

In the Heusler alloys, total spin magnetic moments per formula unit (f.u.) M_t have been reported to follow the generalized Slater–Pauling curve by Galanakis et al., which is represented as $M_t = Z_t - 18$ (half Heusler) and $Z_t - 24$ (full Heusler), where Z_t is the total number of valence band electrons as shown in Fig. 7 [18,19]. This behavior enables us to preferentially control the magnetic properties, the spin DOS at E_F in particular, continuously by substituting the Y atoms with the other transition metals as listed in Fig. 3. Even though there are over 2400 possible combinations to form Heusler alloys, there are about a few tens of alloys reported to become the HMFs according to theoretical calculations on this point (see Tables 1 and 2). For example, a Co_2CrAl alloy has been theoretically calculated to become a HMF [48], however, the T_C has been reported to be around RT (334 K) for bulk [98]. In order to increase the T_C, the substitution of the Cr atoms with the Fe atoms have been successfully reported experimentally [79,81], proving the spin engineering by crystallographical manipulation.

2. Half Heusler alloy films

After the first theoretical prediction of the half-metallicity of the half Heusler NiMnSb alloy [12], this alloy has been intensively investigated to confirm its half-metallicity experimentally. As listed in Table 1, the magnetic moment per formula unit and the bandgap δ are calculated to be approximately 3.99 μ_B/f.u. and 0.5 eV [19], respectively, resulting in calculated spin polarization of 99.3% [20]. For a bulk single crystal, the NiMnSb alloy has indeed been observed to show almost 100% spin polarization at E_F by means of spin-polarized positron-annihilation [26,27]. Both co-sputtering [28] and MBE [29] techniques are employed to grow epitaxial films, which are confirmed mostly by X-ray diffraction (XRD) and magnetocrystalline

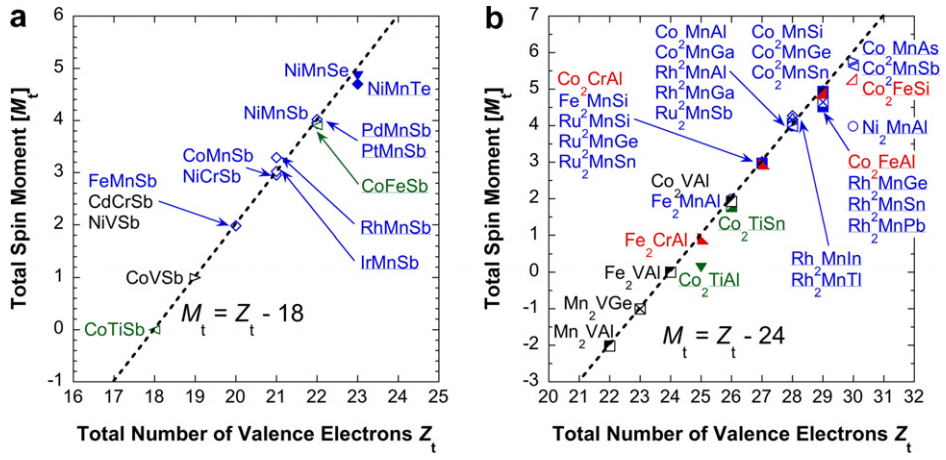

Fig. 7. Calculated total spin moments per formula unit as a function of the total number of valence electrons per formula unit for both (a) half and (b) full Heusler alloys [18,19]. Several Heusler alloys, which are not calculated to show the half-metallicity, are also shown with underlines as references.

Table 1
List of major magnetic properties of half-metallic half Heusler alloys. Italic and roman letters correspond to calculated and experimental values, respectively

Half Heusler alloys	Magnetic moment (μ_B/f.u.)		δ (eV)	T_C (K)	P (%)	Refs.
	Calculation	Experiment				
NiMnSb	*4.00* [12]	3.85 (bulk) [14,21]	*0.5* [19]	*900–1112* [25]	*99.3* [20]	[28–39]
	3.9910 [20]	3.6 (poly) [22]	0.5 [24]	730 (bulk) [14]	58 ± 2.3 [13]	
	3.991 [19]*	3.9 ± 0.2 [23]			~44 [22]	
					~100 [26,27]	
PtMnSb	*4.00* [12]	4.14 (bulk) [14]		582 (bulk) [14]		[33,40]
	3.997 [19]*	3.97 (bulk) [21]				[41]
FeMnSb	*1.930* [42]* [19]*				*99.3* [20]	
CoMnSb	*2.949* [42]* [19]*	4.0 (bulk) [14]	*~1* [19]	*671–815* [25]	*99.0* [20]	[21]
				490 (bulk) [14]		
CoTiSb			*0.95* [43]			
			0.82 [19]			
NiTiSb	*0.0* [43]		*0.14* [19]			
FeVSb			*0.36* [19]			
CoZrSb			*0.83* [19]			

* Calculated total magnetic moments per formula unit, while the others are calculated spin magnetic moments per formula unit.

anisotropy, however, the spin polarization is found to be about only 28% at 0.4 K estimated from TMR [29]. For this alloy film grown in a similar manner, the surface spin polarization P is measured to be only ~58% [13]. This large departure from the bulk property can be explained by the presence of the atomic disorder at the empty sites [30]. The energy gap for the minority spins at E_F is reported to vanish with an atomic disorder of more than 7%. In addition, the surface state is very fragile due to the reduced symmetry and the surface reconstruction [38,39]. On the contrary, epitaxial NiMnSb(100) films are grown on Mo(100) buffers on MgO(111) substrates, showing 67 ± 9 to 100% spin polarization at the MnSb terminated surface, which is much higher than that of 50% for polycrystalline samples, measured by angle-resolved X-ray photoemission [24]. A study on the epitaxial NiMnSb(001) growth on MgO(001) is also performed with using a V(001) buffer layer by Turban et al. [23]. They find the Stransky–Krastanov growth mode under the optimized growth temperature of 620 K. The magnetic moment is estimated to be 3.9 ± 0.2 μ_B/f.u., which agrees almost perfectly with the calculations [12,19,20].

Epitaxial NiMnSb(001) growth on GaAs(001) has been studied systematically by van Roy et al. [31]. They use a low growth temperature (300 K) to avoid interfacial Mn_2As mixing between NiMnSb and GaAs, which may introduce a magnetic dead layer. The lattice constant is slightly enhanced to be 0.5904–0.5909 nm as compared with the bulk value (0.5903 nm) due to the small lattice mismatch with GaAs. Stoichiometric epitaxial NiMnSb films are also grown on GaAs(111)B [34]. These results clearly indicate that the presence of the vacancy sites in the half Heusler alloy (Fig. 2(a)) does not contradict high chemical ordering under precisely controlled deposition. They also find that these films contain very small point defect concentrations: 1.1% Mn planer defects occur in 1 nm thick region in the vicinity of the NiMnSb/GaAsB interface, which agrees very well with calculations that the half-metallic characteristics are recovered within less than 6 atomic planes ($\leqslant$0.7 nm) [32]. For the NiMnSb interfaces, the lattice mismatch is calculated to induce strain: 2% lattice expansion reduces the δ by 0.25 eV, while 2% lattice compression increases the δ by 0.5 eV [21], and the -2 to $+3$% lattice expansion maintains the half-metallicity [35].

In addition to the possible decrease in the half-metallicity due to the atomic disorder and the interface states, which can be overcome by the optimized growth as mentioned above, the surface spin polarization is calculated with respect to the interfaces, the crystalline orientations and the terminated lattice planes. For the NiMnSb(001) surfaces, the Ni-terminated surface compresses the distance between the surface Ni and subsurface MnSb layers by 10% ($P = 42$%), while the MnSb-terminated surface reduces the distance between the surface Mn and subsurface Ni layers by 3.5% and expands that between the surface Sb and subsurface Ni layers by 7.3% ($P = 84$%) [36]. The NiMnSb(111) surfaces, on the other hand, show much larger surface deformation: the Ni-terminated surface shows 23% and 18% reduction in the Ni–Sb and Ni–Mn distances, respectively, reducing the half-metallicity significantly. For the case of a NiMnSb/InP interface, the Mn surface is calculated to increase the spin moment up to 4.0 μ_B, inducing a spin polarization of about 74%, and the Ni/P interface reduces the spin polarization down to 39% for the first two interfacial layers [37].

Similar argument can be applied for the other half Heusler alloy films. PtMnSb films are deposited on Al_2O_3(0001) by sputtering to form spin-valve structures, showing 0.47% giant magnetoresistance (GMR) at RT [40,41]. This may also be due to the empty site disorder. Calculations suggest the decrease in the surface spin polarization dependent upon the terminated layers: $P \sim 46$% and 22% for the MnSb and Pt termination, respectively [33]. The other half Heusler alloy CoMnSb shows similar decrease in the surface spin polarization and the bandgap change by the

Table 2
List of major magnetic properties of half-metallic full Heusler alloys. Italic and roman letters correspond to calculated and experimental values, respectively

Full Heusler alloys	Magnetic moment (μ_B/f.u.)		δ (eV)	T_C (K)	P (%)	Refs.
	Calculation	Experiment				
Co_2MnAl	*4.09* [45] *4.10* [46] *3.970* [18] *4.020* [47] *4.036* [42,19]*	4.01 (bulk) [14]	*0.306* [48]	693 (bulk) [14]	42 [49]† 58 [52]†	[50] [51] [53]
Co_2MnSi	*5.00* [45] *4.96* [54] *4.940* [18] *5.0* [55] *5.008* [42,19]*	5.07 (bulk) [14] 5.10 ± 0.04 (bulk) [56] 4.95 ± 0.25 [57] 4.7 [58] 5.0 [59] 5.1 [60]	*0.419* [48] *0.81* [55]	*740–857* [25] 985 (bulk) [14] 690 [15]	54 ± 3 [57] 35 [58]† 89 [61]††	[53]
Co_2MnGa	*4.14* [45] *4.21* [46] *3.72* [54] *4.058* [18]	4.05 (bulk) [14]		694 (bulk) [14]	∼50 [62]	[63]
Co_2MnGe	*5.00* [45] *4.84* [54] *4.941* [18] *5.0* [55] *5.012* [42,19]*	5.11 (bulk) [14] 4.93 (bulk) [64] 5.1 [65]	*0.210* [48] *∼0.5* [45]	905 (bulk) [14]		[66] [67]
Co_2MnSn	*5.03* [45] *4.78* [54] *4.984* [18] *5.0* [55] *5.043* [47] *5.089* [42,19]*	5.08 (bulk) [14]	*0.174* [48]	829 (bulk) [14]		[53]
Co_2CrAl	*2.99* [45] *2.955* [18] *3.007* [47] *3.0* [35] *2.999* [19]* *2.96–3.01* [68] *2.970* [69]	1.55 (bulk) [14] 1.5–3 [70] 0.53 [71]	*0.18* [35] *0.75* [68] *0.18* [69]	334 (bulk) [14] 330 [71]	*∼100* [35] *∼97* [72] *∼98* [69] 16 [73]†	[74] [75] [76] [77] [78]
$Co_2Cr_{0.6}Fe_{0.4}Al$	*3.7* [74]	3.4 (bulk) [79] 3.65 (bulk) [80] 2.04 [81] 3.5 [70] 3.1 [73] 3.2 (RT) (bulk) [82], 3.49 (bulk) [83] 3.3 [84] 2.26 (RT) this study	∼0.4 [68]	750 (bulk) [79] 665 ± 2 (bulk) [80]	*∼90* [72] *∼95* [69] 18 [81]† 25 [80]† 29 [73]†	
(Co_2FeAl)	*4.996* [45] *4.98* [46] *4.98* [18] *4.996* [19]* *4.811* [69]	4.9 [70] 4.8 [71] 5.29 [83]	*0.1* [68]	1170 (bulk) [17]	*∼30* [72] 46 [73]†	[74] [75] [78]
Co_2CrGa	*3.01* [46]	3.01 (bulk) [85]		495 (bulk) [85]	*95* [85]	
Co_2FeSi						[86]
Co_2NiGa		3.21 (bulk) [14]		670 [15]		
Co_2TiAl	*1.00* [87]		*0.438* [87]	135 (bulk) [88]		
Co_2TiSi	*2.00* [87]		*0.800* [87]			
Co_2TiGa	*1.00* [87]		*0.157* [87]			
Co_2TiGe	*2.00* [87]		*0.602* [87]			
Co_2TiSn	*1.85* [54] *1.784* [18] *2.00* [87] *1.68* [90]	1.93 (bulk) [14] 1.92 (bulk) [90]	*0.478* [87] 0.0123 [89]	*359* [54] 359 (bulk) [14] ∼350 (bulk) [89]		
Co_2ZrSn	*1.64* [90]	1.64 (bulk) [90]				
Co_2NbSn	*1.08* [90]	0.94 (bulk) [90]				
(Co_2TiSb)	*1.73* [87]		*0.567* [87]			

(*continued on next page*)

Table 2 (*continued*)

Full Heusler alloys	Magnetic moment (μ_B/f.u.)		δ (eV)	T_C (K)	P (%)	Refs.
	Calculation	Experiment				
Co_2FeGa	*5.15* [54]			>1100 [54]		
(Ni_2MnAl)				~350 [91]		
(Ni_2MnGa)				~320 [92]		[97]
				~350 [93]		
				~340 [94]		
(Ni_2MnGe)				~320 [94,95]		
(Ni_2MnIn)				~170 (*B2*) [96]		

* Calculated total magnetic moments per formula unit, while the others are calculated spin magnetic moments per formula unit. Spin polarization values with † and †† are estimated at RT and 2 K, respectively, by using Jullière's formula [44]. Several non-half-metallic full Heusler alloys are also shown in brackets as references.

strain: +2% and −2% lattice deformation shifts the δ by −0.8 eV and +0.9 eV, respectively [21].

3. Full Heusler alloy films

3.1. Co-based full Heusler alloys

3.1.1. Co_2MnZ

A pioneering work on the growth of full Heusler alloy films has been performed for a Co_2MnGe/GaAs(0 0 1) hybrid structure by Ambrose et al. [65]. They obtain an epitaxial Co_2MnGe film with a slightly enhanced lattice constant as compared with bulk. The magnetic moment is estimated to be 5.1 μ_B/f.u., which almost perfectly agrees with the bulk value (see Table 2). For this alloy, calculations suggest that the strong reduction of the magnetic moment may occur near the Co_2MnGe/GaAs interface due to the Co–As and Co–Ga bonding [67].

Consequently, systematic search has been widely carried out over Co_2Mn-based full Heusler alloys to realize the RT half-metallicity; Co_2MnAl [49–53], Co_2MnSi [53,56–61], Co_2MnGa [62,63] and Co_2MnSn [53]. For Co_2MnAl, an epitaxial film has been grown on a Cr buffer layer by sputtering with the crystalline relationship $Co_2MnAl(0\,0\,1)[1\,1\,0]\|Cr(0\,0\,1)[1\,1\,0]\|MgO(0\,0\,1)[1\,0\,0]$ but with the *B*2 structure [50]. For Co_2MnSi, the $L2_1$ structure has been deposited by using both dc magnetron sputtering [57,58,60,61] and MBE [59]. Some of these films are used as electrodes in magnetic tunnel junctions (MTJs) and recently show large TMR ratios at low temperature, which is discussed in Section 5.2.

Calculations imply that the strain induced in the unit cell can control the half-metallicity in the Co_2MnZ alloys. For Co_2MnSi for example, the lattice compression of 4% in the lattice constant increases the δ by 23%, and a similar behavior is expected for the other alloy compounds [55]. In other calculations, ±2% change in the lattice constant preserves the half-metallicity in the Co_2MnZ alloys [19].

3.1.2. $Co_2(Cr,Fe)Al$

Block et al. have presented large negative magnetoresistance (MR) at RT in a quarternary full Heusler $Co_2Cr_{0.6}Fe_{0.4}Al$ alloy [79], which firmly proves the controllability of the spin DOS of the full Heusler alloys by substituting their constituent elements. They report −30% MR at RT with pressed powder compacts, which acts as a series of MTJs. As a result, a great amount of attempts has been made to utilize this alloy system to achieve large MR due to the half-metallic characteristics [70,73,80,81]. For example an epitaxial film is deposited on a MgO(0 0 1) substrate with the crystalline relationship $Co_2Cr_{0.6}Fe_{0.4}Al(0\,0\,1)[1\,0\,0]\|MgO(0\,0\,1)[1\,1\,0]$, showing only 2% GMR at RT (4% at 15 K) [70].

The influence of the atomic disorder on the half-metallicity for the $Co_2Cr_{1-x}Fe_xAl$ full Heusler alloys has been systematically studied by Shirai et al. by using first-principles calculations [72,74,75]. In the Co_2CrAl alloys, the atomic disorder between Cr and Al, which eventually deforms the crystalline structure from $L2_1$ into *B*2 at a disorder level of 0.5, maintains the very high spin polarization *P*; 97% for $L2_1$ and 93% for *B*2 [72]. The Co–Cr type disorder, however, destroys the half-metallicity rapidly: *P* falls to zero at a disorder level of 0.4 and the magnetic moment becomes 2.0 μ_B/f.u. at the full disorder. For the Fe substitution x with Cr, *P* is calculated to stay above 90% up to $x = 0.35$. Similarly, in the $Co_2Cr_{1-x}Fe_xAl$ alloys, the CrFe–Al type disorder preserves both *P* and the magnetic moment to be above 80% and 3.7 μ_B/f.u., respectively, up to the disorder level of 0.5, while the Co–CrFe disorder eliminates *P* at the disorder level of 0.3 [74]. These findings may explain the decrease in the estimated magnetic moments in the earlier study [81].

Strain also affects the half-metallicity in the Co_2CrAl alloy according to calculations [35]. *P* stays ~100% in the lattice strain range between −1 and +3%, and is even higher than 90% under +10% strain. The δ is also robust against the strain and can be maximized under +3% strain. *P* also remains ~100% against the tetragonal distortion in the range of ±2%, which is a great advantage for the epitaxial growth study on a GaAs substrate.

We have therefore grown stoichiometric epitaxial $Co_2Cr_{1-x}Fe_xAl$ films directly onto GaAs(0 0 1) substrates by using three-source co-evaporation with an ultrahigh vacuum (UHV) MBE technique: two *e*-guns to evaporate Co and $Cr_{1-x}Fe_x$, and a K-cell to evaporate Al at the ratio of $Co:Cr_{1-x}Fe_x:Al = 2:1:1.76$ ($x = 0$, 0.4 and 1). We have already reported structural and magnetic properties of both polycrystalline Co_2CrAl/GaAs and epitaxial $L2_1$

$Co_2FeAl(001)/GaAs(001)$ hybrid structures [71]. The Co_2FeAl film grown at 673 K forms an almost perfect $L2_1$ structure for the thickness above 7.5 nm, of which crystalline relationship is $Co_2FeAl(001)\langle 110\rangle \| GaAs(001)\text{-}110\rangle$ unambiguously supported by *in situ* reflection high-energy electron diffraction (RHEED) observation together with *ex situ* XRD measurement (typically within 1% distortion as compared with the bulk value). The film shows strong uniaxial anisotropy along the [1 −1 0] direction with a magnetic moment of 4.8 μ_B/f.u. Even though the TMR ratio for this film is only 9% at RT, the growth condition for this Heusler alloy system has been successfully optimized.

Here we extend this study and investigate for $x = 0.4$ films grown directly on GaAs(001). As shown in Fig. 8, *in situ* RHEED patterns reveal the detailed growth mechanism and confirm the formation of the $L2_1$ structure. Both the zeroth and first order Laue spots, corresponding to the $A2$ structure, appear above the thickness of 1.2 nm (2 ML using the lattice constant estimated by XRD, 0.576 nm) (closed circles in Fig. 8(a)). Both the 1/2 order superlattice spots (closed squares in Fig. 8(b)) and another set of the superlattice spots, such as $(1/2, 0)$ and $(-1/2, 0)$ (crosses in Fig. 8(b)), then emerge above 2.0 nm (3.5 ML), representing the formation of the $L2_1$ structure. Although this initial thickness to form the $L2_1$ structure is found to be thinner than that for Co_2FeAl [71], the epitaxial relationship is the same as for the Co_2FeAl; $Co_2Cr_{0.6}Fe_{0.4}\text{-}Al(001)\langle 110\rangle \| GaAs(001)\langle 110\rangle$ (see Fig. 8(d) and (e)). Since the Co atoms are reported to favorably adhere to the GaAs surface [75], only the Co/As interface is drawn in this figure for the ideal case. The $L2_1$ structure is stable with further film deposition up to 20 nm with very clean surface (streak lines in Fig. 8(c)), which is ideal for the device applications. Even though the half-metallicity should be preserved at the Co/As interface on the (001) surface [75], initial growth of the $A2$ structure of 3.5 ML may introduce unfavorable interfaces, such as the CrAl/As, to reduce the half-metallicity in the vicinity of the interface.

Fig. 9(a) shows the magnetization curves for the epitaxial $L2_1$ $Co_2Cr_{0.6}Fe_{0.4}Al$ film. As clearly seen, strong uniaxial anisotropy along the [1 −1 0] axis is observed with the hard axes of [1 0 0] and [0 1 0] directions. Along the [1 1 0] direction, minor steps are obtained during the magnetization reversal at the magnetic field of $\sim\pm 20$ Oe, indicating that the magnetization once lies along the easy axis [1 −1 0] during the reversal as previously observed for the epitaxial Co_2MnGe [65] and Co_2FeAl [71] films. The magnetic moment is estimated to be 2.26 μ_B/f.u. at RT, which is 70% of the bulk value (3.2μ_B/f.u. at RT) [82]. In order to investigate this reduction, element specific magnetic moments are measured by using X-ray magnetic circular dichroism (XMCD). The details of the measurement are

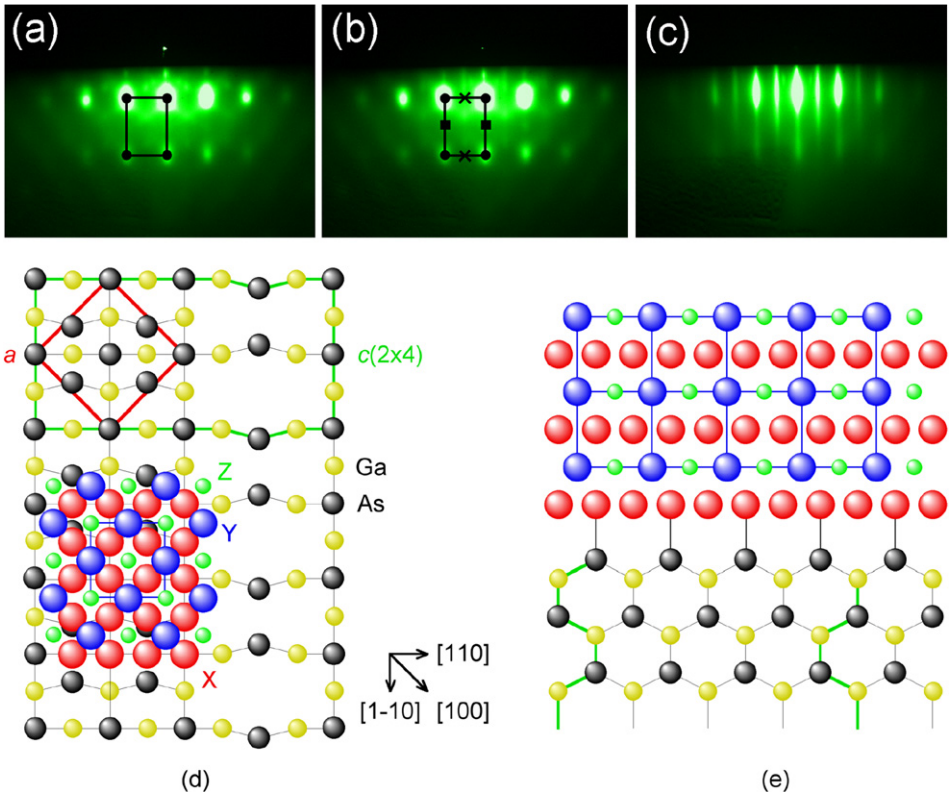

Fig. 8. RHEED patterns along the [1 1 0] azimuth of the $Co_2Cr_{0.6}Fe_{0.4}Al$ film deposited on a GaAs(001) substrate at the temperature of 673 K, of which thickness is (a) 1.2, (b) 2.0 and (c) 20 nm. Schematic illustrations of the epitaxial growth of a full Heusler alloy film on a GaAs substrate; (d) top view over the (001) plane and (e) sideview along the [1 1 0] axis.

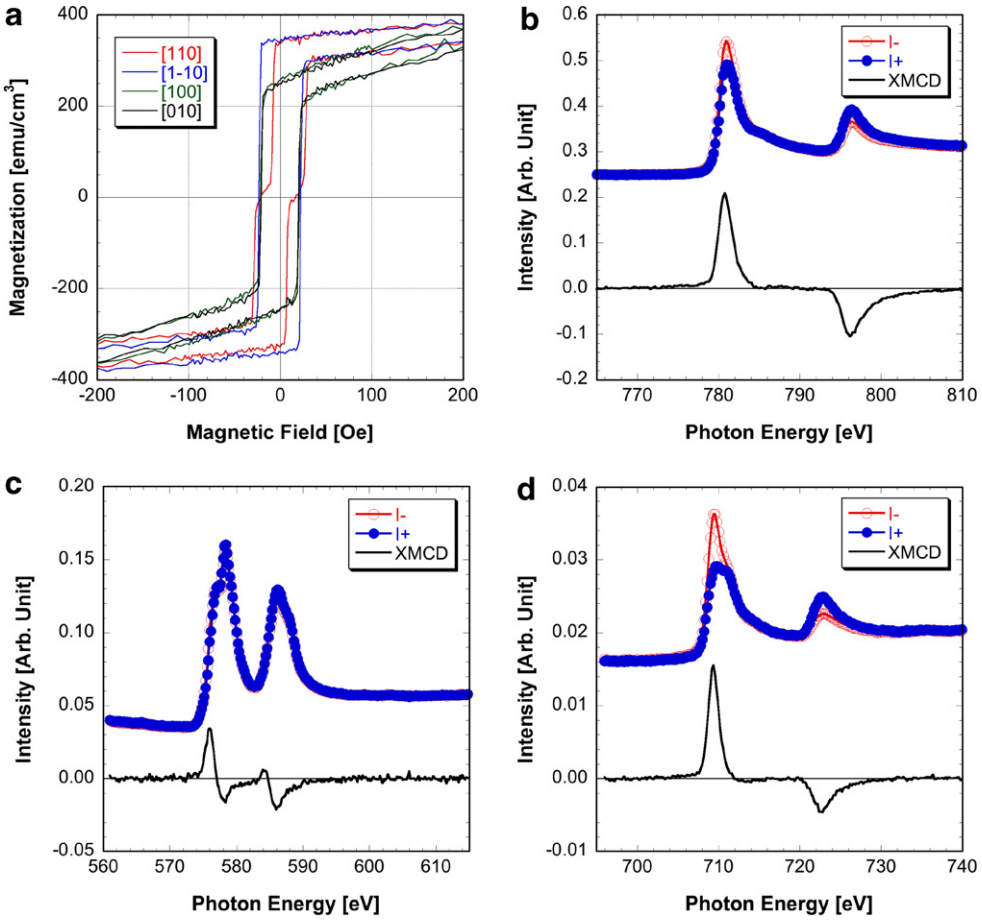

Fig. 9. (a) Magnetization curves as a function of an applied magnetic field for the 20 nm thick $Co_2Cr_{0.6}Fe_{0.4}Al(001)/GaAs(001)$ hybrid structure measured at RT. Normalized XMCD spectra of the $Co_2Cr_{0.6}Fe_{0.4}Al$ film for (b) Co, (c) Cr and (d) Fe absorption edges. XAS spectra for opposite polarizations, I^- (lines with open circles) and I^+ (lines with closed circles), are also shown.

described in Section 4.3 and in the earlier study [78]. As shown in Fig. 9(c) and (d), the X-ray absorption spectroscopy (XAS) spectra for both Cr and Fe possess minor splits in the peaks, corresponding to the oxidation of these elements. For Co, on the other hand, no peak splitting is observed and the spin magnetic moment per atom is estimated to be 1.09 μ_B (Fig. 9(b)), which almost agrees with the calculated value (0.96 μ_B) [82]. These results suggest that the epitaxial $L2_1$ $Co_2Cr_{0.6}Fe_{0.4}Al$ film suffers from element selective oxidation at the interface with a 3 nm thick MgO capping layer (used in this study to compare the magnetic properties directly with those in a MTJ), resulting in the decrease in the spin magnetic moments for Cr and Fe.

3.2. Ni-based full Heusler alloys

Even though Ni_2MnZ alloys are not predicted to become HMFs by calculations, detailed studies on epitaxial growth on GaAs and InAs has been reported by Palmstrøm et al. [15]. By using a $Sc_{0.3}Er_{0.7}As$ buffer layer on GaAs(001), both Ni_2MnAl [91] and Ni_2MnGa [92,94] films are epitaxially grown. Although Ni_2MnGa films are also epitaxially grown directly on GaAs(001) with the crystalline relationship $Ni_2MnGa(001)[100,010]\|GaAs(001)[100,010]$, no strong in-plane magnetocrystalline anisotropy is observed in their magnetization curves [93]. $Ni_2MnGe(001)/GaAs(001)$ [94,95] and $Ni_2MnIn(001)/InAs(001)$ [96] hybrid structures are additionally fabricated. The interfaces are reported to be very sensitive to the growth temperature: interfacial mixture occurs at the growth temperature of 373 K, while a large number of planer defects are formed e.g., at 433 K for $Ni_2MnGe/GaAs$ [94]. All these films are slightly tetragonally elongated along the plane normal as compared with the bulk values due to the minor lattice mismatch with the semiconductor substrates, and eventually the Ni_2MnIn film on InAs transforms into the $B2$ structure. First-principles calculations demonstrate that a broad energy minimum of tetragonal Ni_2MnGa can explain stable pseudomorphic growth of Ni_2MnGa on GaAs despite a nominal 3% lattice mismatch [97].

4. Major characterizations

4.1. X-ray diffraction

For the XRD analysis, one predominantly focuses on both superlattice peaks, (111) and (200), and the principal peak (220). The appearance of all three peaks corresponds

to the formation of the $C1_b$ or $L2_1$ structures in the sample, while the disappearance of the (1 1 1) peak represents that of the $B2$ structure and that of both the superlattice peaks indicates that of the $A2$ structure for the full Heusler alloys according to the XRD intensity calculation as described below. For the $L2_1$ structure with the X_2YZ Heusler alloys, the structure amplitudes of the XRD reflection for the (1 1 1), (2 0 0) and (2 2 0) peaks are given by $F(111) = 4|f_Y - f_Z|$, $F(200) = 4|2f_X - (f_Y + f_Z)|$ and $F(220) = 4|2f_X + (f_Y + f_Z)|$, respectively, where f_M (M = X, Y and Z) are the average scattering factors for the M atoms [99]. The principal reflection (2 2 0) satisfies the relationship $(h + k + l)/2 = 2n$ (h, k and l: Miller indices, and n: integer), and is not affected by the atomic disorder. When the disorder occurs absolutely randomly among the M atoms, the magnitude of the first two superlattice peaks are reduced by the factor S^2, where S is the degree of long range order described using the number of the X atoms on the $L2_1$-ordered X sites n_X as $S = \{n_X - n_X(A2)\}/\{n_X(L2_1) - n_X(A2)\}$ ($S = 1$ for the $L2_1$ structure). When the Y–Z disorder occurs, the second peak (2 0 0) with $(h + k + l)/2 = 2n + 1$ is not affected, while the first peak with h, k and l are all odd is reduced by a factor of $(1 - 2a)S^2$, where a is a disorder parameter defined as the fraction of the Y atoms occupying the Z sites ($a = 0.5$ for the $B2$ structure). By using the structure amplitudes $F(hkl)$, the XRD peak intensity $I(hkl)$ is calculated as follows: $I(hkl) = |F(hkl)|^2 p\{(1 + \cos^2 2\theta)/\sin^2\theta\cos\theta\}$ (p: multiplicity factor) [100]. For the polycrystalline Co_2CrAl alloy for instance, the peak intensity ratio normalized by the principal (2 2 0) reflection is calculated to be $I(111):I(200):I(220) = 5:6:100$, while this is 7:5:100 for the polycrystalline Co_2FeAl alloy [71]. Comparison of these calculated values with experimental observations provides a measure of the atomic ordering in the Heusler alloy samples, however, cannot be applied directly to the epitaxial films.

4.2. Electrical resistivity

As the other macroscopic measure to assess the half-metallicity, electrical resistivity is commonly measured as a function of temperature, $\rho(T)$. In general, the temperature dependence of the resistivity can be written as $\rho(T) = \rho(4\text{ K}) + cT^m$, where m is an exponent factor. In a conventional ferromagnetic metal, since one-magnon scattering (or electron–electron scattering) dominates the resistivity at low temperature, m becomes 2 theoretically [101]. For the HMF, due to the 100% spin polarization, the one-magnon scattering is suppressed by the factor of $\exp(-\delta/k_BT)$ (δ is energy bandgap for the minority spins at E_F and k_B is Boltzmann constant), leading to typically $m = 1.5$ at low temperature. At a finite temperature, spin fluctuation activates the minority band and unconventional one-magnon scattering starts to happen, which is described as $m = 3$.

Experimentally, the $\rho(T)$ of an epitaxial NiMnSb film follows a $T^{1.55}$ law below 100 K, which clearly indicates the absence of spin-flip electron diffusion due to the half-metallic property [23]. For the full Heusler alloys, on the other hand, $\rho(T)$ is observed to be almost constant at low temperature, while m is measured to be $m = 1.5$ and 1.2 ± 0.1 at a finite temperature below RT in single-crystal Co_2MnGe [65] and polycrystalline Co_2MnGa films [63], respectively. Co_2CrAl bulk similarly shows $m = 3.15$ at low temperature but 1.33 above 35 K [77]. Epitaxial Co_2FeAl films show $m = 2.6$ below 50 K but 1.3 above 100 K [70], and $m = 4.2$ below 30 K but 1.5 above 115 K [71]. For Co_2MnSi films [57], a relationship $\rho(T) = T^2 + T^{4.5}$ is found, which may consist of an electron–electron scattering term T^2 and a two-magnon scattering term $T^{4.5}$. Such a departure from the ideal law observed in the full Heusler alloys especially at low temperature is mainly attributed to the presence of grain boundaries in the films, for the case of the polycrystalline films in particular [56].

The residual resistivity ratio (RRR) $\rho(300\text{ K})/\rho(4\text{ K})$ can also be used to characterize the bulk properties of the half-metallic films. For Co_2MnGa [63] and Co_2CrAl [71], the normalized resistivity $\rho(T)/\rho(4\text{ K})$ has been reported to decrease monotonically with increasing T, providing the RRR to be less than 1, a behavior which is common for highly resistive materials, such as an intrinsic semiconductor. For most of the Heusler films, the RRR is obtained to be 1.28 for a single-crystal Co_2MnGe film [65] and 1.3 for epitaxial $L2_1$ Co_2FeAl film [71], which is much smaller than that observed for e.g., a Co_2MnSi bulk single crystal (6.5) [56] and for Co_2TiAl bulk (4.2) [88]. Since a very large RRR is reported for the bulk single crystal due to the improvement of the crystallinity of the alloy at low temperature, the small RRRs for the Heusler films may indicate the stable crystallinity against temperature change. By comparing the RRR with the $\rho(T)$, an epitaxial Heusler alloy film without grain boundaries is expected to show the ideal $\rho(T)$ behavior.

4.3. X-ray magnetic circular dichroism

As a direct method to estimate the element specific magnetic moments per atom, XMCD has been exploited. The XMCD measurements are performed at the L_2 and L_3 absorption edges of the constituent elements of the Heusler alloys, which represent the X-ray-induced excitation from the $2p_{1/2}$ and $2p_{3/2}$ core levels into the valence d states, respectively [102]. A magnetic field is applied perpendicular to the sample films, realizing the magnetization of the samples parallel (or antiparallel) to the incident circularly polarized X-rays. These two configurations provide the corresponding X-ray absorption spectra, both of which are measured by using the total electron yield method, revealing the difference in the population between up and down spin electrons. The difference in absorption cross sections represents the XMCD signals as a result (see Fig. 9(b)–(d) for example). Since the orbital part of the atomic wavefunction interacts with the circularly polarized X-rays [103], which indirectly interact with the spins of the

atoms through the spin–orbit interaction [104], non-zero XMCD signals are observed in the vicinity of the L_2 and L_3 edges. By applying the sum rules [103–105], after relevant background subtraction, element specific spin magnetic moments per atom m_{spin} are estimated as listed in Table 3. For all the samples, the m_{spin} for the element X agrees very well with the calculated values within ±20%, while that for Y is smaller than the calculations by 26–86%. This considerable reduction does not depend on the form of the samples (bulk or film). Because the XMCD measurement is sensitive to the surface of the sample, typically probing within 10 nm from the surface, the measurement always suffers from the overlap of the surface signals with the bulk signals. For the bulk samples, the asymmetry at the surface reduces the m_{spin} in addition to the strain induced by the surface cleaning process [83]. For the films, the asymmetry and dislocation in the vicinity of the interfaces between the Heusler alloy layers and the capping layers, which are usually deposited to prevent oxidation, reduce the m_{spin}. In the form of a MTJ, selective oxidation also reduces the m_{spin} as discussed in Section 3.1.2.

Recently, Elmers et al. have reported the orbital magnetic moment per spin, $r = m_{orb}/(m_{spin} + m_{dipole})$, to be (0.14 ± 0.02) for Co and (0.06 ± 0.02) for Fe in the Co_2FeAl bulk samples [82,83]. For the $L2_1$ epitaxial Co_2FeAl films, by neglecting the magnetic dipole term, m_{dipole}, r is estimated to be (0.098 ± 0.007) and (0.069 ± 0.005) for Co and Fe, respectively [78]. These values imply that Co does not show any enhancement in the m_{orb}, while Fe shows similar enhancement as the bulk. Even so, it should be emphasized that the m_{orb} for Co in the epitaxial films is observed to be twice as large as the calculation (see Table 3). Similar enhancement in the m_{orb} for Co has been reported in a Co_2MnGe bulk sample [64]. Such enhancement in the m_{orb} for the transition metals X and Y suggests that the spin–orbit coupling in the Heusler alloys are very strong and may be the main reason to induce the half-metallicity. For sputtered Co_2MnAl film with the atomically disordered $B2$ structure, the Gilbert damping constant is found to be small by ferromagnetic resonance (FMR) measurement, indeed indicating weak spin–orbit interaction for the disordered phases [51]. The large spin–orbit interaction in the Heusler alloys has also been suggested from a large AMR effect observed in polycrystalline Co_2MnGa film, as large as 6% at RT (8% at 1.6 K) [63].

4.4. Andreev reflection

Soulen et al. have first applied Andreev reflection to measure the spin polarization P of metals [13], and afterwards this technique has been widely used to measure the P of the Heusler alloys as listed in Tables 1 and 2. Meservey and Tedrow have pioneered the estimation of P by spectroscopic measurement in a ferromagnet/insulator/superconductor tunnel junction [106]. For Andreev reflection, a superconducting point contact is used instead, which allows one spin-polarized electron injection into a normal metal sample with forming a coherent pair with an oppositely spin-polarized electron in the metal, while reflecting an Andreev hole back to the superconductor. This process occurs in addition to the conventional ohmic response at the interface. The HMF, for which P is 100%, however, cannot offer the coherent pair when the majority spin is injected from the point contact due to the absence of the minority spins at E_F in the HMF. Although this is a very powerful technique to measure P directly, the estimated P typically reflects the spin DOS in the vicinity of the surface.

5. Applications

5.1. Spin injection

In order to achieve highly efficient spin injection from a ferromagnet into a semiconductor or a non-magnetic metal, two distinct approaches have been proposed theoretically; spin injection from the ferromagnet with almost 100% spin polarization, such as a DMS and a HMF, in a diffusive regime [107], and that through a tunnel barrier in a ballistic regime [108]. For the former case, the Heusler alloy is one of the best candidates due to their good lattice matching with major semiconductors and their high T_C as discussed above. Diffusive spin injection holds a key to realize the spin-polarized three-terminal devices at RT.

A NiMnSb(1 1 1)/CdS(1 1 1) interface is suggested to suppress the spin-flip electron transport at E_F [32], indicating the possibility of using the NiMnSb film as a spin-filter to inject a spin-polarized electron current into the semiconductor. A similar effect is expected even for the electron transport in the [1 1 0] orientation in a non-half-metallic Ni_2MnIn/InAs interface, resulting in $P \sim 80\%$ [109]. At this interface, only the electron spins within an energy of $k_BT \approx 1/40$ eV at E_F in Ni_2MnIn are transported into InAs. E_F must be close to the conduction band of InAs for the spins to fill these unoccupied states. Since the conduction minimum occurs at the Γ point, the transmittances for the minority spins are calculated to be 0.75, 0.82 and 0.99 for the [1 0 0], [1 1 0] and [1 1 1] directions, respectively. For the majority spins, on the other hand, since large spin–orbit scattering is expected at the interface to change the in-plane momentum to match an available state in InAs, the transmittances are calculated to be 0.19, 0.19 and 0.39 for the corresponding directions.

For the case of the Co_2CrAl/III–V semiconductor interfaces, the half-metallicity is calculated to be preserved for certain combinations. For Co_2CrAl/GaAs interfaces, the half-metallicity is preserved for the Co/As interface on the GaAs(0 0 1) surface and for Al/As on GaAs(1 1 0), while it is demolished for e.g., CrAl/As on GaAs(0 0 1) [75]. For Co_2CrAl/InP interfaces, the Cr spin moment is calculated to be enhanced for both the CrAl/In and CrAl/P interfaces ($P \sim 63\%$ and 65%, respectively), while it is decreased for both the Co/In and Co/P interfaces ($P \sim 56\%$ and ~74%,

Table 3
List of element specific magnetic moments per atom for both full and half Heusler alloys

Hesuler alloys		Total magnetic moment (μ_B/f.u.)	X (μ_B/atom)		Y (μ_B/atom)		Refs.
			m_{orb}	m_{spin}	m_{orb}	m_{spin}	
NiMnSb	Experiment	3.9 ± 0.2		0.2		3.0	[23]
	Calculation	*3.991*	*0.015*	*0.245*	*0.027*	*3.720*	[19]
Co_2MnSi	Experiment	4.7		1.20 ± 0.05		~2.6	[23]
	Calculation	*5.008*	*0.029*	*0.994*	*0.017*	*3.022*	[19]
$Co_2Cr_{0.6}Fe_{0.4}Al$ (bulk)	Experiment	3.49	0.12	0.96	Cr: 0.04 Fe: 0.33	Cr: 0.40 Fe: 2.37	[82,83]
	Calculation			*0.96*		Cr: *1.52* Fe: 2.77	
$Co_2Cr_{0.6}Fe_{0.4}Al$	Experiment	2.26 (RT)	0.038 ± 0.004	1.09 ± 0.11	Cr: – Fe: –	Cr: – Fe: –	This study
$Co_2Cr_{0.625}Fe_{0.375}Al$	*Calculation*	*3.68*	0.021–0.048	0.764–0.0.923	Cr: *0.001*–0.010 Fe: *0.028*–0.083	Cr: *1.244*–0.1.537 Fe: *2.469*–2.787	[69]
Co_2FeAl	Experiment	4.8	0.089 ± 0.003	0.91 ± 0.04	0.089 ± 0.005	1.29 ± 0.05	[71,78]
	Calculation	*4.996*	*0.045*	*1.094*	*0.060*	*2.753*	[19]
Co_2TiSn (bulk)	Experiment	1.92	0.09 ± 0.02	0.87 ± 0.02			[90]
	Calculation	*1.68*		*0.90*			
Co_2ZrSn (bulk)	Experiment	1.64	0.012 ± 0.01	0.70 ± 0.01			
	Calculation	*1.64*		*0.88*			
Co_2NbSn (bulk)	Experiment	0.94	0.09 ± 0.01	0.38 ± 0.01			
	Calculation	*1.08*		*0.43*			

respectively), even though the Cr spin moment is almost the same as the bulk value [76].

Experimentally, spin injection has been reported in a $Co_{2.4}Mn_{1.6}Ga$/InGaAs quantum well (QW) structure [62]. Although P is observed to be ~50% by using the Andreev reflection, the injected electron spin polarization is measured to be 13% at 5 K, which is smaller than that for an Fe/InAs QW. It is therefore essential to fabricate a sharp Heusler alloy/semiconductor interface with a relevant band matching as theoretically suggested in order to achieve highly efficient spin injection.

5.2. Magnetic tunnel junctions

Recent achievement of over 100% TMR ratios at RT with oriented MgO barriers [110,111] has offered major progress in improving areal density of a magnetic random access memory (MRAM), which is the other important spintronic device. Such a giant TMR effect has theoretically been predicted due to the Δ_1 band connection at the Fe(001)/MgO interface only for the majority spins [112,113]. In contrast with such coherent tunneling, the Heusler alloy films have been widely applied as electrodes in the conventional MTJs in order to obtain a very large TMR ratio at RT due to their large P.

An epitaxial half Heusler NiMnSb film has been first used as an electrode in a MTJ, showing 9% TMR at RT [29]. An epitaxial full Heusler Co_2FeAl film with the $L2_1$ structure is also applied for a MTJ but shows only 9% TMR at RT [71]. These small TMR ratios may be caused by the selective oxidation at the interface between the Heusler films and the oxide barriers as discussed in Section 3.1.2. Recently, an epitaxial $L2_1$ $Co_2Cr_{0.6}Fe_{0.4}Al$ film sputtered onto MgO(001) substrate has been adopted for a fully epitaxial MTJ with the structure of $Co_2Cr_{0.6}Fe_{0.4}Al$/MgO/CoFe, showing 42% at RT (74% at 55 K) [84]. Even though this film possesses the crystalline relationship $Co_2Cr_{0.6}Fe_{0.4}Al(001)[100]||MgO(001)[110]$, the magnetic moment is estimated to be 3.3 μ_B/f.u., which is smaller than the calculation (3.7 μ_B/f.u.) [74]. This indicates that the film contains an atomically disordered phase, which may also be suggested from the decrease in the TMR ratios below 55 K, resulting in the reduction in the TMR ratio.

For polycrystalline sputtered full Heusler MTJs, on the other hand, higher TMR ratios have been reported. A MTJ with the structure of $Co_2Cr_{0.6}Fe_{0.4}Al/AlO_x$/CoFe shows 16% TMR at RT [81], which is later improved up to 19% at RT by the barrier optimization [73]. Similarly, a MTJ with Co_2MnAl/AlO_x/CoFe shows 40% TMR at RT [49], followed by the further improvement up to 61% at RT (83% at 2 K) [52]. All of these Heusler films in the MTJs have been reported to be $B2$ structure. By comparing the TMR ratios at RT with those at low temperature, the ratios are found to show very weak temperature dependence as similarly observed for a conventional metallic MTJ. On the contrary, a MTJ with a highly ordered Co_2MnSi film shows strong temperature dependence; 33% at RT and 86% at 10 K [58], and 70% at RT and 159% at 2 K [61]. Such rapid decrease in the TMR ratio with increasing temperature does not follow the temperature dependence of the magnetization, suggesting that small fraction of atomically disordered phases cannot be ignored in the spin-polarized electron transport at a finite temperature. The elimination of such disordered phases especially near the barrier interface improves the TMR ratios further and realizes the half-metallicity at RT.

Theoretical calculations also suggest that the interface states within the half-metallic bandgap at the half-metal/insulator interfaces prevent the highly spin-polarized electron transport [114]. This is because the tunneling rate is slower than the spin-flip rate, and therefore the interface states for the minority spins are effectively coupled to the metallic spin reservoir of the majority spin states. In order to avoid the spin-flip scattering, a sharp interface without the interface states is crucially required.

6. Summary

In a Heusler alloy/III–V semiconductor hybrid structure, the spin DOS in the Heusler film is engineered by the interface states in addition to the crystallographical manipulation by the element substitution in the film. Although recent progress in the film growth techniques enables researchers to fabricate an almost perfectly ordered Heusler film on a semiconductor, typically a few ML of minor atomic disorder at both the interface and the surface prevents to achieve half-metallicity at RT, which has been theoretically predicted for a bulk Heusler alloy. In order to eliminate the interface states and to minimize the surface asymmetry, first-principles calculations are employed, suggesting that the half-metallicity is maintained in relevant combinations of interfacial atomic bonding, a surface termination and a crystalline orientation. Such an atomically controlled Heusler film is highly required for the use as a spin source for future spintronic devices.

Acknowledgements

The authors thank Prof. Y. Otani (University of Tokyo and RIKEN) and Dr. S.N. Holmes (Toshiba Research Europe) for fruitful discussion.

References

[1] Prinz GA. Magnetic metal films on semiconductor substrates. In: Heinrich B, Bland JAC, editors. Ultrathin magnetic structures II. Berlin: Springer; 1994. p. 1.
[2] Moodera JS, Meservey RH. Spin-polarized tunneling. In: Johnson M, editor. Magnetoelectronics. Amsterdam: Elsevier; 2004. p. 163.
[3] Ohno H. Ferromagnetic III–V semiconductors and their heterostructures. In: Awschalom DD, Loss D, Samarth N, editors. Semiconductor spintronics and quantum computation. Berlin: Springer; 2002. p. 1;
Schmidt G, Molenkamp LW. Electrical spin injection: spin-polarized transport from magnetic into non-magnetic semiconductors.

In: Awschalom DD, Loss D, Samarth N, editors. Semiconductor spintronics and quantum computation. Berlin: Springer; 2002. p. 93.
[4] Datta S, Das B. Appl Phys Lett 1990;56:665.
[5] Jonker BT, Park YD, Bennet BR, Cheong HD, Kioseoglou G, Petrou A. Phys Rev B 2000;62:8180.
[6] Gruber T, Keim M, Fiederling R, Ossau G, Schmidt G, Molenkamp LW. Appl Phys Lett 2001;78:1101.
[7] Galanakis I, Dederichs PH, editors. Half-metallic alloys. Berlin: Springer; 2005.
[8] Schwarz K. J Phys F 1986;16:L211.
[9] Yamase A, Shiratori K. J Phys Soc Jpn 1984;53:312.
[10] Okimoto Y, Katsufuji T, Ishikawa T, Urushibara A, Arima T, Tokura Y. Phys Rev Lett 1995;75:109.
[11] Akinaga H, Manago T, Shirai M. Jpn J Appl Phys 2000;39:L1118.
[12] de Groot RA, Mueller FM, van Engen PG, Buschow KHJ. Phys Rev Lett 1983;50:2024.
[13] Soulen Jr RJ, Byers JM, Osofsky MS, Nadgorny B, Ambrose T, Cheng SF, et al. Science 1998;282:85.
[14] Webster PJ, Ziebeck KRA. Heusler Alloys. In: Wijn HRJ, editor. Landolt-Börnstein new series group III, vol. 19C. Berlin: Springer; 1988. p. 75.
[15] Palmstrøm C. MRS Bull 2003;28:725.
[16] Yoshimura K, Miyazaki A, Vijayaraghavan R, Nakamura Y. J Magn Magn Mater 1985;53:189.
[17] Kobayashi K, Umetsu RY, Kainuma R, Ishida K, Oyamada T, Fujita A, et al. Appl Phys Lett 2004;85:4684.
[18] Galanakis I, Dederichs PH, Papanikolaou N. Phys Rev B 2002;66:174429.
[19] Galanakis I, Mavropoulos P, Dederichs PH. J Phys D: Appl Phys 2006;39:765.
[20] Mavropoulos P, Galanakis I, Popescu V, Dederichs PH. J Phys: Condens Matter 2004;16:S5759.
[21] van Engen PG, Buschow KHJ, Jongebreur R. Appl Phys Lett 1983;42:202.
[22] Clows SK, Miyoshi Y, Bugoslavsky Y, Branford WR, Gringorescu C, Manea SA, et al. Phys Rev B 2004;69:214425.
[23] Turban P, Andrieu S, Kierren B, Snoeck E, Teodorescu C, Traverse A. Phys Rev B 2002;65:134417.
[24] Ristoiu D, Nozières JP, Borca CN, Komesu T, Jeong H-K, Dowben PA. Europhys Lett 2000;49:624.
[25] Şaşğlu E, Sandratskii LM, Bruno P, Galanakis I. Phys Rev B 2005;72:184415.
[26] Hanssen KEHM, Mijnarends PE. Phys Rev B 1986;34:5009.
[27] Hanssen KEHM, Mijnarends PE, Rabou LPLM, Buschow KHJ. Phys Rev B 1990;42:1533.
[28] Mancoff FB, Bobo JF, Richter OE, Bessho K, Johnson PR, Sinclair R, et al. J Mater Res 1999;14:1560.
[29] Tanaka CT, Nowak J, Moodera JS. J Appl Phys 1999;86:6239.
[30] Orgassa D, Fujiwara H, Schulthess TC, Butler WH. Phys Rev B 1999;60:13237.
[31] van Roy W, de Boeck J, Brijs B, Borghs G. Appl Phys Lett 2000;77:4190.
[32] de Wijs GA, de Groot RA. Phys Rev B 2001;64:R020402.
[33] Galanakis I. J Phys: Condens Matter 2002;14:6329.
[34] van Roy W, Wójcik M, Jędryka E, Nadolski S, Brijs B, Borghs G, et al. Appl Phys Lett 2003;83:4214.
[35] Block T, Carey MJ, Gurney BA, Jepsen O. Phys Rev B 2004;70:205114.
[36] Ležaić M, Galanakis I, Bihlmayer G, Blügel S. J Phys: Condens Matter 2005;17:3121.
[37] Galanakis I, Ležaić M, Bihlmayer G, Blügel S. Phys Rev B 2005;71:214431.
[38] Jenkins SJ, King DA. Surf Sci 2001;494:L793.
[39] Jenkins SJ. Phys Rev B 2004;70:245401.
[40] Johnson PR, Kautzky MC, Mancoff FB, Kondo R, Clemens BM, White RL. IEEE Trans Magn 1996;32:4615.
[41] Kautzky MC, Mancoff FB, Bobo J-F, Johnson PR, White RL, Clemens BM. J Appl Phys 1997;81:4026.
[42] Galanakis I. Phys Rev B 2005;71:012413.
[43] Toboła J, Pierre J, Kaprzyk S, Skolozdra RV, Kouacou MA. J Phys: Condens Matter 1998;10:1013.
[44] Jullière M. Phys Lett 1975;54A:225.
[45] Fujii S, Sugimura S, Ishida S, Asano S. J Phys: Condens Matter 1990;2:8583.
[46] Ishida S, Sugimura S, Fujii S, Asano S. J Phys: Condens Matter 1991;3:5793.
[47] Galanakis I. J Phys: Condens Matter 2004;16:3089.
[48] Ishida S, Fujii D, Kashiwagi S, Asano S. J Phys Soc Jpn 1995;64:2152.
[49] Kubota H, Nakata J, Oogane M, Ando Y, Sakuma A, Miyazaki T. Jpn J Appl Phys 2004;43:L984.
[50] Sakuraba Y, Nakata J, Oogane M, Kubota H, Ando Y, Sakuma A, et al. Jpn J Appl Phys 2005;44:6535.
[51] Yilgin R, Oogane M, Yakata S, Ando Y, Miyazaki T. IEEE Trans Magn 2005;41:2799.
[52] Sakuraba Y, Nakata J, Oogane M, Ando Y, Kato H, Sakuma A, et al. Appl Phys Lett 2006;88:022503.
[53] Geiersbach U, Bergmann A, Westerholt K. J Magn Magn Mater 2002;240:546.
[54] Brown PJ, Neumann KU, Webster PJ, Ziebeck KRA. J Phys: Condens Matter 2000;12:1827.
[55] Picozzi S, Continenza A, Freeman AJ. Phys Rev B 2002;66:094421.
[56] Raphael MP, Ravel B, Huang Q, Willard MA, Cheng SF, Das BN, et al. Phys Rev B 2002;66:104429.
[57] Singh LJ, Barber ZH, Miyoshi Y, Branford WR, Cohen LF. J Appl Phys 2004;95:7231.
[58] Kämmerer S, Thomas A, Hütten A, Reiss G. Appl Phys Lett 2004;85:79.
[59] Wang WH, Przybylski M, Kuch W, Chelaru LI, Wang J, Lu YF, et al. Phys Rev B 2005;71:144416.
[60] Singh LJ, Barber ZH, Kohn A, Petford-Long AK, Miyoshi Y, Bugoslavsky Y, et al. J Appl Phys 2006;99:013904.
[61] Sakuraba Y, Nakata J, Oogane M, Kubota H, Ando Y, Sakuma A, et al. Jpn J Appl Phys 2005;44:L1100.
[62] Hickey MC, Damsgaard CD, Farrer I, Holmes SN, Husmann A, Hansen JB, et al. Appl Phys Lett 2005;86:252106.
[63] Holmes SN, Pepper M. Appl Phys Lett 2002;81:1651.
[64] Miyamoto K, Kimura A, Iori K, Sakamoto K, Xie T, Moko T, et al. J Phys: Condens Matter 2004;16:S5797.
[65] Ambrose T, Krebs JJ, Prinz GA. Appl Phys Lett 2000;76:3280.
[66] Hoshiya H, Hoshino K. J Appl Phys 2004;95:6774.
[67] Picozzi S, Continenza A, Freeman AJ. J Phys Chem Solids 2003;64:1697.
[68] Fecher GH, Kandpal HC, Wurmehl S, Morais J, Lin H-J, Elmers H-J, et al. J Phys: Condens Matter 2005;17:7237.
[69] Antonov VN, Dürr HA, Kucherenko Y, Bekenov LV, Yaresko AN. Phys Rev B 2005;72:054441.
[70] Kelekar R, Clemens BM. J Appl Phys 2004;96:540.
[71] Hirohata A, Kurebayashi H, Okamura S, Kikuchi M, Masaki T, Nozaki T, et al. J Appl Phys 2005;97:103714.
[72] Miura Y, Nagao K, Shirai M. Phys Rev B 2004;69:144413.
[73] Okamura S, Goto R, Sugimoto S, Tezuka N, Inomata K. J Appl Phys 2004;96:6561.
[74] Miura Y, Shirai M, Nagao K. J Appl Phys 2004;95:7225.
[75] Nagao K, Shirai M, Miura Y. J Phys: Condens Matter 2004; 16:S5725.
[76] Galanakis I. J Phys: Condens Matter 2004;16:8007.
[77] Zhang M, Liu Z, Hu H, Liu G, Cui Y, Chen J, et al. J Magn Magn Mater 2004;277:130.
[78] Hirohata A, Kurebayashi H, Okamura S, Masaki T, Nozaki T, Kikuchi M, et al. J Appl Phys 2005;97:10C308.
[79] Block T, Felser C, Jakob G, Ensling J, Mühling B, Gütlich P, et al. J. Solid State Chem 2003;176:646.

[80] Clifford E, Venkatesan M, Gunning R, Coey JMD. Solid State Commun 2004;131:61.
[81] Inomata K, Okamura S, Goto R, Tezuka N. Jpn J Appl Phys 2003;42:L419.
[82] Elmers HJ, Fecher GH, Valdaitev D, Nepijko SA, Gloskovskii A, Jakob G, et al. Phys Rev B 2003;67:104412.
[83] Elmers HJ, Wurmehl S, Fecher GH, Jakob G, Felser C, Schönhense G. Appl Phys A 2004;79:557.
[84] Marukame T, Kasahara T, Matsuda K-I, Uemura T, Yamamoto M. IEEE Trans Magn 2005;41:2603.
[85] Umetsu RY, Kobayashi K, Kainuma R, Fujita A, Fukamichi K, Ishida K, et al. Appl Phys Lett 2004;85:2011.
[86] Hashimoto M, Herfort J, Schönherr H-P, Ploog KH. Appl Phys Lett 2005;87:102506.
[87] Lee SC, Lee TD, Blaha P, Schwarz K. J Appl Phys 2005;97: 10C307.
[88] Zhang W, Qian Z, Sui Y, Liu Y, Huang X, Su W, et al. Physica B 2005;367:205.
[89] Majumdar S, Chattopadhyay MK, Sharma VK, Sokhey KJS, Roy SB, Chaddah P. Phys Rev B 2005;72:012417.
[90] Yamasaki A, Imada S, Arai R, Utsunomiya H, Suga S, Muro T, et al. Phys Rev B 2002;65:104410.
[91] Dong XY, Dong JW, Xie JQ, Shih TC, McKernan S, Leighton C, et al. J Cryst Growth 2003;254:384.
[92] Dong JW, Chen LC, Palmstrøm CJ, James RD, McKernan S. Appl Phys Lett 1999;75:1443.
[93] Dong JW, Chen LC, Xie JQ, Müller TAR, Carr DM, Palmstrøm CJ, et al. J Appl Phys 2000;88:7357.
[94] Dong JW, Lu J, Xie JQ, Chen LC, James RD, McKernan S, et al. Physica E 2001;10:428.
[95] Lu J, Dong JW, Xie JQ, McKernan S, Palmstrøm CJ, Xin Y. Appl Phys Lett 2003;83:2393.
[96] Xie JQ, Dong JW, Lu J, Palmstrøm CJ, McKernan S. Appl Phys Lett 2001;79:1003.
[97] Godlevsky VV, Rabe KM. Phys Rev B 2001;63:134407.
[98] Buschow KHJ, van Engen PG. J Magn Magn Mater 1981;25:90.
[99] Webster PJ. J Phys Chem Solids 1971;32:1221.
[100] Cullity BD. Elements of X-ray diffraction. second ed. Reading (MA): Addison Wesley; 1977.
[101] Furukawa N. J Phys Soc Jpn 2000;69:1954.
[102] Lovesey SW, Collins SP. X-ray absorption by magnetic materials. Oxford: Oxford University Press; 1996.
[103] Thole BT, Carra P, Sette F, van der Laan G. Phys Rev Lett 1992; 68:1943.
[104] Carra P, Thole BT, Altarelli M, Wang X. Phys Rev Lett 1993; 70:694.
[105] Chen CT, Idzerda YU, Lin H-J, Smith NV, Meigs G, Chaban E, et al. Phys Rev Lett B 1995;75:152.
[106] Tedrow PM, Meservey R. Phys Rep 1994;238:173.
[107] Schmidt G, Ferrand D, Molenkamp LW, Filip AT, van Wees BJ. Phys Rev B 2000;62:R4790.
[108] Rashba EI. Phys Rev B 2000;62:R16267.
[109] Kilian KA, Victora RH. J Appl Phys 2000;87:7064.
[110] Parkin SSP, Kaiser C, Panchula A, Rice PM, Hughes B, Samant M, et al. Nat Mater 2004;3:862.
[111] Yuasa S, Nagahama T, Fukushima A, Suzuki Y, Ando K. Nat Mater 2004;3:868.
[112] Butler WH, Zhang X-G, Schulthess TC. Phys Rev B 2001;63:054416.
[113] Mathon J, Umerski A. Phys Rev B 2001;63:R220403.
[114] Mavropoulos P, Ležaić M, Blügel S. Phys Rev B 2005;72:174428.